Synergistic catalytic effect of N-doped carbon embedded with CoFe-rich CoFe$_2$O$_4$ clusters as highly efficient catalyst towards oxygen reduction

Mancai Qian [a, b], Xiaoyang Cheng [a], Tingting Sun [a], Jianniao Tian [a], Tayirjan Taylor Isimjan [c, **], Zhongfeng Shi [a, b, ***], Xiulin Yang [a, *]

[a] Guangxi Key Laboratory of Low Carbon Energy Materials, School of Chemistry and Pharmaceutical Sciences, Guangxi Normal University, Guilin, 541004, People's Republic of China
[b] College of Petroleum and Chemical Engineering, Beibu Gulf University, Qinzhou, 535011, People's Republic of China
[c] Saudi Arabia Basic Industries Corporation (SABIC) at King Abdullah University of Science and Technology (KAUST), Thuwal, 23955-6900, Saudi Arabia

ARTICLE INFO

ABSTRACT

Spinel cobalt ferrite is one of the promising electrocatalysts for the ORR, but the poor electrical conductivity limits its application. Herein, we report a simple and efficient method to synthesize the N-doped carbon-shielding CoFe-rich CoFe$_2$O$_4$ catalyst which exhibits superior ORR catalytic activity under alkaline conditions due to the improved conductivity and high electrochemically active surface area. The NC@CoFe−CoFe$_2$O$_4$ catalyst shows a positive onset potential (1.0 V), half-wave potential (0.89 V) and maximum limiting current density (−5.0 mA cm^{-2}), which are similar to commercial Pt/C, while significantly higher than those of all other controls and most of the previously reported catalysts. The Koutecky-Levich equation and rotating ring-disk electrode test prove a direct four-electron reduction process. Moreover, the NC@CoFe−CoFe$_2$O$_4$ catalyst also demonstrates superior methanol tolerance and long-term stability compared to Pt/C. The proposed catalytic mechanism analysis illustrates that the excellent ORR electrocatalytic activities and durability are the combined effect of highly conductive CoFe alloy, abundant Co−N/Fe−N sites along with the hydrophilic nature of CoFe$_2$O$_4$ clusters.

© 2019 Elsevier B.V. All rights reserved.

1. Introduction

The ever-increasing demand for renewable energy to replace fossil fuels has invited substantial attention in the community [1,2]. Despite the fact that significant progress has been made on sustainable energy storage and conversion systems, including fuel cells and metal-air batteries, the sluggish kinetics of oxygen reduction reaction (ORR) at the cathode is the main barriers limiting the performance of these systems [3−6]. To date, the state-of-the-art noble metal catalysts are commonly used as ORR catalysts. However, their high cost, scarcity, durability, and methanol crossover pose a severe limitation to global-scale applications [7−10]. Thus, exploring nonprecious metal catalysts (NPMCs) with high ORR activity, excellent durability, and resistant to methanol is an alternative road to reducing cost and realizing the commercial application of energy conversion technology.

In the past decades, developing the first-row (3d) transition-metal-based oxygen reduction electrocatalysts with comparable performance to Pt/C attracted tremendous attention because of their promising ORR activity, low-cost, and high stability [11−13]. Among them, the transition-metal-based spinel metal oxides from Fd3m space group were explored as a new class of compounds with mixed valence, which shows interesting electrocatalytic activities toward ORR in alkaline [14]. However, this type of oxide is a semiconductor and easily aggregated during continuous operation, catalysts composed of these nanoclusters are usually supported on carbon-based materials with high conductivity [15,16] or they are modified by various physical treatments. For instance, Liu et al. reported that FeCo$_2$O$_4$ nanoparticles with abundant oxygen vacancies via laser fragmentation could lower not only the

* Corresponding author.
** Corresponding author.
*** Corresponding author. Guangxi Key Laboratory of Low Carbon Energy Materials, School of Chemistry and Pharmaceutical Sciences, Guangxi Normal University, Guilin, 541004, People's Republic of China.
E-mail addresses: isimjant@sabic.com (T.T. Isimjan), shizhongfeng01@163.com (Z. Shi), xlyang@gxnu.edu.cn (X. Yang).

thermodynamic energy barriers but also accelerate the electron transfer [17]. Zhang's group reported $NiFe_2O_4$ quantum dots anchored carbon nanotubes with appealing ORR and OER activity [18]. Furthermore, Liu et al. also revealed a Ni-NiM_2O_4 (M = Mn or Fe) supported on N-doped CNTs that exhibits a robust trifunctional catalytic performance towards HER, OER, and ORR in alkaline electrolyte [19]. However, the ORR activity of the materials is still far from that of the commercial Pt/C. However, the ORR activities of those materials are still far from that of the commercial Pt/C. It has been reported that the ORR performance of spinel metal oxides can be improved significantly by incorporating nitrogen-doped carbon [20] due to the enhanced binding energies between the active species and supports with the N-participation [21]. Meanwhile, the synergistic interaction favors the high dispersion and modification of electronic states for the active species.

We found that the N-doped carbon-based hybrid materials feature the high specific surface area and high conductivity, which are beneficial to the charge (ions and electrons) transfer and mass transport [22], Thus it exhibits a high potential for advanced energy conversion and storage applications. As a result, the NC@Co-Fe–$CoFe_2O_4$ catalyst achieved a high ORR performance with a half-wave potential of 0.89 V (vs. RHE, the same hereafter), more positive than these of NC@Fe–Fe_3O_4 (0.84 V) and NC@Co–CoO (0.85 V), reaching a record-high value for the Fe-based spinel metal oxides. The stability of the NC@CoFe–CoFe2O4 catalyst is superior to the commercial Pt/C, with a comparable ORR activity. This result indicates the possibility of using the low cobalt-content bimetallic oxide as the potential inexpensive catalyst to enhance cathodic performance.

2. Experimental section

2.1. Synthesis of C@CoFe-species

Initially, 1.2 g urea and 1.5 g D-glucose are dispersed into a mixture solution containing 30 mL H_2O and 20 mL ethylene glycol. Then, 2.0 mmol Co(NO_3)$_2$·$6H_2O$ and 4.0 mmol Fe(NO_3)$_3$·$9H_2O$ are slowly added into the above mixture solution under continuous stirring. Thirty minutes later, the resulting mixture was transferred into a Teflon-lined stainless-steel autoclave with a capacity of 100 mL. The autoclave was then heated to 180 °C for 12 h in an electric oven. After cooling to room temperature naturally, the precipitate was harvested by centrifugation, washed with a large amount of DI water, and then freeze-dried overnight to prepare the C@CoFe-species composite. Moreover, the pure CoFe-species, C@Fe-species and C@Co-species were also prepared as above except that glucose, Co(NO_3)$_2$ or Fe(NO_3)$_3$ was not added. The carbon spheres were prepared by directly hydrothermal aqueous glucose solution, as mentioned above.

2.2. Synthesis of NC@CoFe–$CoFe_2O_4$

The NC@CoFe–$CoFe_2O_4$ material was prepared by continuous two-step calcination. In which a certain amount of C@CoFe-species and melamine (mass ratio of 10:1) was firstly heated to 250 °C and kept for 2 h in N_2 atmosphere, and then subsequently heated to a specific temperature (600, 700 or 800 °C) with a fixed heating rate of 5 °C min^{-1} and kept for another 1 h. After cooling to room temperature, the calcined sample was collected and nominated as NC@CoFe–$CoFe_2O_4$ (XRD data). In addition, the catalytic control materials of NC@Fe–Fe_3O_4, NC@Co–CoO, NC and $CoFe_2O_4$ composites were also prepared under similar experimental conditions as discussed above using C@Fe-species, C@Co-species, carbon spheres, and CoFe-species, as the precursor materials, respectively.

2.3. Reference electrode calibration

In order to convert the data tested in the electrochemical system using Ag/AgCl as a reference electrode to a standard hydrogen electrode (RHE), we performed a test calibration. First, high-purity H_2 gas was continuously bubbled into electrolyte for 30 min to form a H_2-saturated 0.1 M KOH solution. Second, cyclic voltammetry was performed using two clean Pt foils and one Ag/AgCl (KCl saturated) electrode as working, counter, and reference electrodes, respectively. The average of the two potentials at which the current crossed zero was taken to be the thermodynamic potential for the reactions (See Fig. S1 for details).

2.4. Preparation of catalytic electrode

The synthesized catalyst (4.0 mg) and Nafion solution (5 wt%, 50 μL) were ultrasonically dispersed in ethanol (950 μL) for half an hour to obtain a homogeneous suspension. 10 μL of catalyst ink was pipetted on the surface of a clean glassy carbon electrode (GC, diameter for 5.0 mm) and rotating ring-disk electrode (RRDE, disk diameter 5.61 mm), dried in air to obtain the working electrodes. The loading of the catalyst is *ca.* 0.20 mg cm^{-2}.

2.5. Electrochemical measurements

The ORR activity was evaluated in a three-electrode system with a carbon rod as the counter electrode, and Ag/AgCl saturated with KCl as the reference electrode, respectively. All electrochemical tests were performed at 25 °C in O_2- or N_2-saturated 0.1 M KOH, which was kept bubbling during the measurements to ensure the O_2- or N_2-saturated electrolyte. Cyclic voltammograms (CVs) were performed in O_2- or N_2-saturated 0.1 M KOH with a scan rate of 50 mV s^{-1}. Linear sweep voltammetry (LSV) tests were performed in O_2-saturated 0.1 M KOH solution with a scan rate of 5 mV s^{-1} at various rotation rates from 625 to 2500 rpm. The methanol cross-over tolerance of the catalyst was evaluated by chronoamperometry measurement in O_2-saturated 0.1 M KOH solution, and 3.0 M CH_3OH was quickly added into the solution after running *ca.* 300 s. The stability test was performed by comparing the LSV curves in O_2-saturated 0.1 M KOH before and after 2000 cycles with a rotation speed of 1600 rpm.

3. Results and discussion

3.1. Synthetic strategy analysis

As shown in Scheme 1, the NC@CoFe–$CoFe_2O_4$ was synthesized through a facile two-step method (details given in Experimental Section). In the first step, ferric nitrate, cobalt nitrate, urea, and glucose were dissolved in the mixed solvents of DI water and ethylene glycol. Afterward, the C@CoFe-species was obtained under a hydrothermal condition at 180 °C. During the solvothermal process, cobalt and ferric nitrates were used as metal and urea as the nitrogen sources [23,24]. After the hydrothermal reaction, the formed CoFe-species clusters are enchased in the carbon layers. In the second step, the freeze-dried powder was calcined at 250 °C then 700 °C under N2 atmosphere. During the calcination process, CoFe-species was partially reduced into CoFe alloy by carbonation and partially converted to CoFe2O4 clusters by oxidation during the pyrolysis. Melamine decomposes at high temperature, and CoFe alloy promotes in-situ growth of carbon nanotubes [25], which are expected to significantly enhance the catalytic activity and stability of catalyst towards ORR due to the high conductivity (Table S1). Besides, a series of control materials are also prepared, such as NC, $CoFe_2O_4$, NC@Fe–Fe_3O_4, and NC@Co–CoO, which contribute
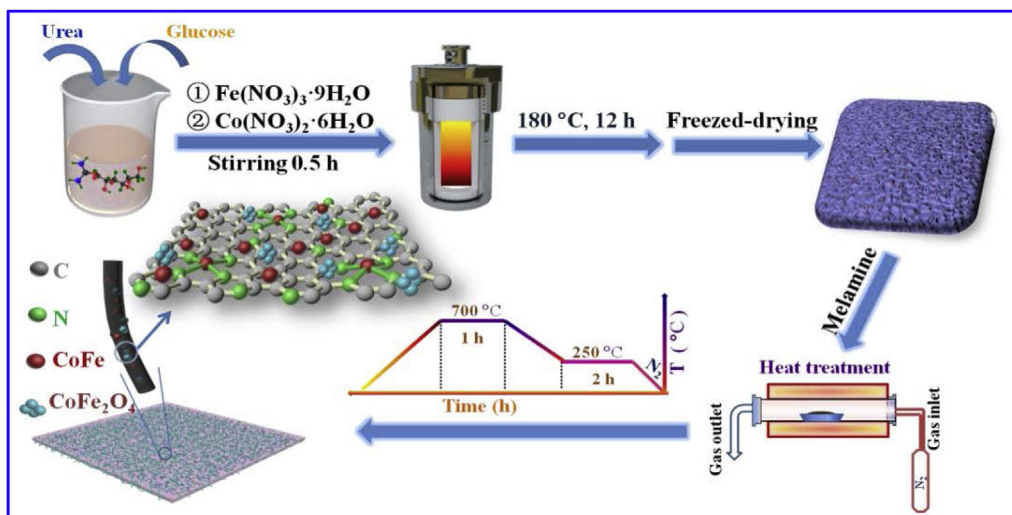
Scheme 1. Synthesis protocol of NC@CoFe−CoFe$_2$O$_4$ catalyst.

significantly to the interpretation of the catalytic mechanism.

3.2. Morphology, compositions and thermal studies

The morphology of the synthesized NC@CoFe−CoFe$_2$O$_4$ was initially characterized by scanning electron microscopy (SEM) and transmission electron microscopy (TEM). The SEM image (Fig. 1a) indicates that there were few curved carbon nanotubes on the carbon layer that resulted in the catalytic effect of CoFe alloy during

the calcination process, similar to that reported previously [26]. The TEM image in Fig. 1b displays that the CoFe alloy and CoFe$_2$O$_4$ clusters are anchored into the N-doped carbon layer of the carbon nanotubes. Typically, the crystal lattices with spacings of 0.21, 0.25 and 0.34 nm are observed in a high-resolution TEM image, which can be attributed to the (110) plane of Co$_3$Fe$_7$ (Fig. 1c), (113) plane of CoFe$_2$O$_4$ and (002) plane of graphitized carbon (Fig. 1d), respectively. Notably, the CoFe particles were wrapped by N-doped carbon layers (Fig. 1c). Fig. 1e further validates the homogeneous
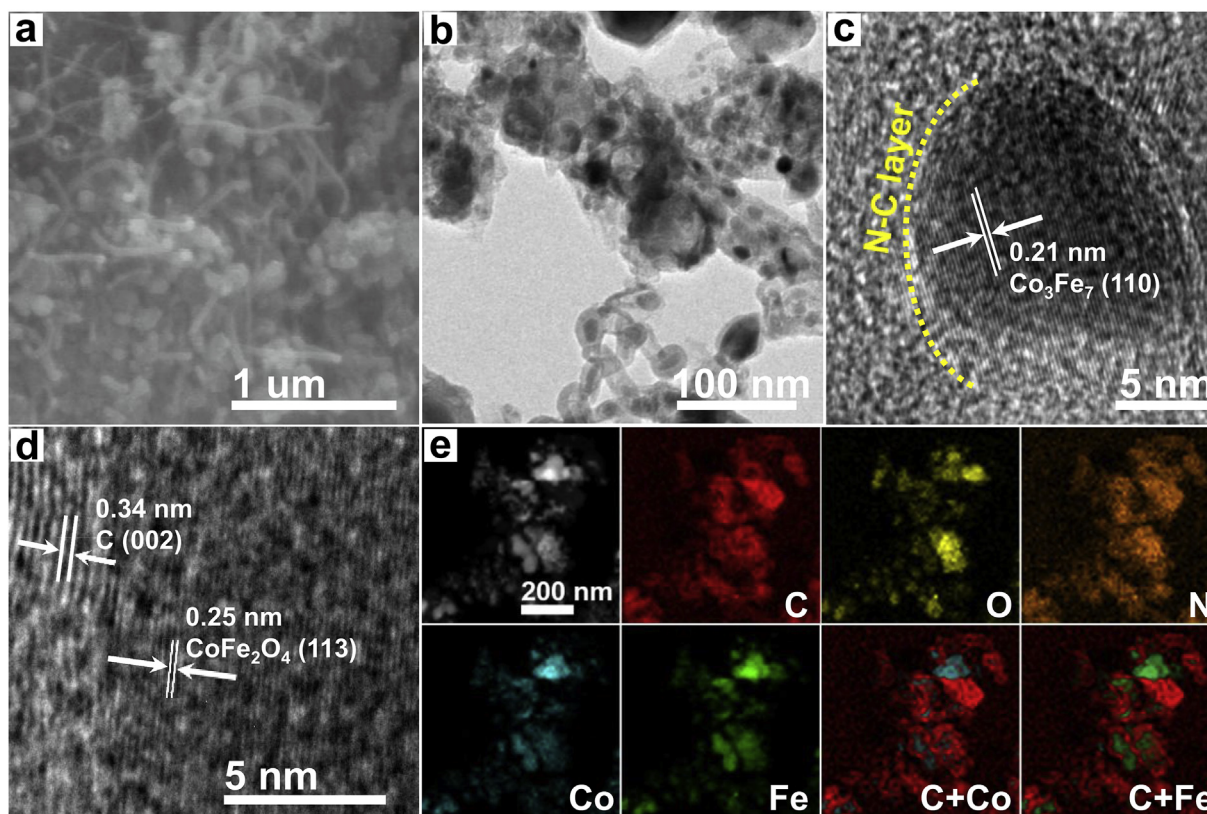

Fig. 1. (a) SEM image and (b) TEM image of NC@CoFe−CoFe$_2$O$_4$. (c−d) High-resolution TEM image of NC@CoFe−CoFe$_2$O$_4$. (e) High-angle annular dark-field (HAADF) TEM image and the corresponding elemental mappings of C, O, N, Co, Fe in the selected area.

elemental distribution of C, O, N, Co, and Fe in the whole structure of NC@CoFe−CoFe₂O₄, and the Co and Fe species are well encapsulated by N-doped carbon layers, implying a high density of active sites.

The crystalline structures of NC@CoFe−CoFe₂O₄ synthesized at different temperatures, together with NC@Fe−Fe₃O₄, NC@Co−CoO, and NC are further examined by XRD patterns. As shown in Fig. 2a, all the three samples exhibit clear diffraction peaks, indicating good crystallinity. The weak peak at ~26° is relevant to the (002) plane of the graphitic carbon structure (JCPDS: 89−8487). The XRD patterns of the NC@CoFe−CoFe₂O₄ (600, 700 and 800 °C) show three distinct peaks at around 44.8°, 65.2°, and 82.5°, which are corresponding to the (110), (200), and (211) crystal planes of Co_3Fe_7 (JCPDS: 48−1817), while the other characteristic peaks at about 30.1°, 35.4°, 43.1°, 56.9°, and 62.5° are well matched with (104), (113), (024), (125), and (208) lattice planes of spinel $CoFe_2O_4$ (JCPDS: 79−1744). It is worth noting that the NC@CoFe−CoFe₂O₄ (700 °C) appears a much stronger and broader diffraction peak at ~44.8° than others, which probably means a high content of CoFe alloy. As a comparison, the NC@Fe−Fe₃O₄ and NC@Co−CoO are also

characterized by XRD patterns (Fig. S2). We can observe that the NC@Fe−Fe₃O₄ contains the cubic structure of Fe_3O_4 (JCPDS: 75−0449) in addition to metallic Fe, while the NC@Co−CoO has α−phase Co (JCPDS: 89−4307) and CoO (JCPDS: 70−2856). These different species and crystallinity could be the critical factors affecting the catalytic performance.

Raman spectroscopy is a non-destructive tool to investigate the structure and graphitization degree of carbon materials. As shown in Fig. 2b, all of the samples display two predominant peaks at about 1350 and 1580 cm^{-1}, corresponding to the D and G bands, respectively. The D-band is assigned to the breathing mode of κ-point phonons of A_{1g} symmetry with vibrations of the carbon atoms of the disordered and defected graphite [27]. The G band is related to E_{2g} phonons of sp^2 carbon atoms [15]. The NC@Co-Fe−CoFe₂O₄ possesses a smaller ratio of I_D/I_G (~0.93) than those of NC@CoFe−CoFe₂O₄-600 (~0.97) and NC@CoFe−CoFe₂O₄-800 (~0.98), indicating a higher graphitization due to the catalytic growth of carbon nanotubes by CoFe alloy. The I_D/I_G of NC@Fe−Fe₃O₄, NC@Co−CoO, and N/C are respective 0.96, 0.92 and 1.0 (Fig. S3), implying that metal-doping can increase the degree of
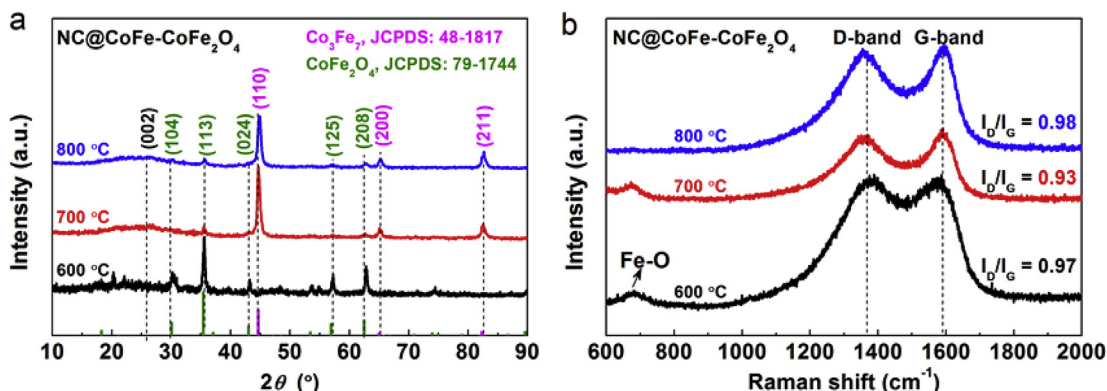

Fig. 2. The XRD patterns (a) and Raman spectra (b) of NC@CoFe−CoFe₂O₄ materials synthesized at different temperatures (600, 700 and 800 °C).
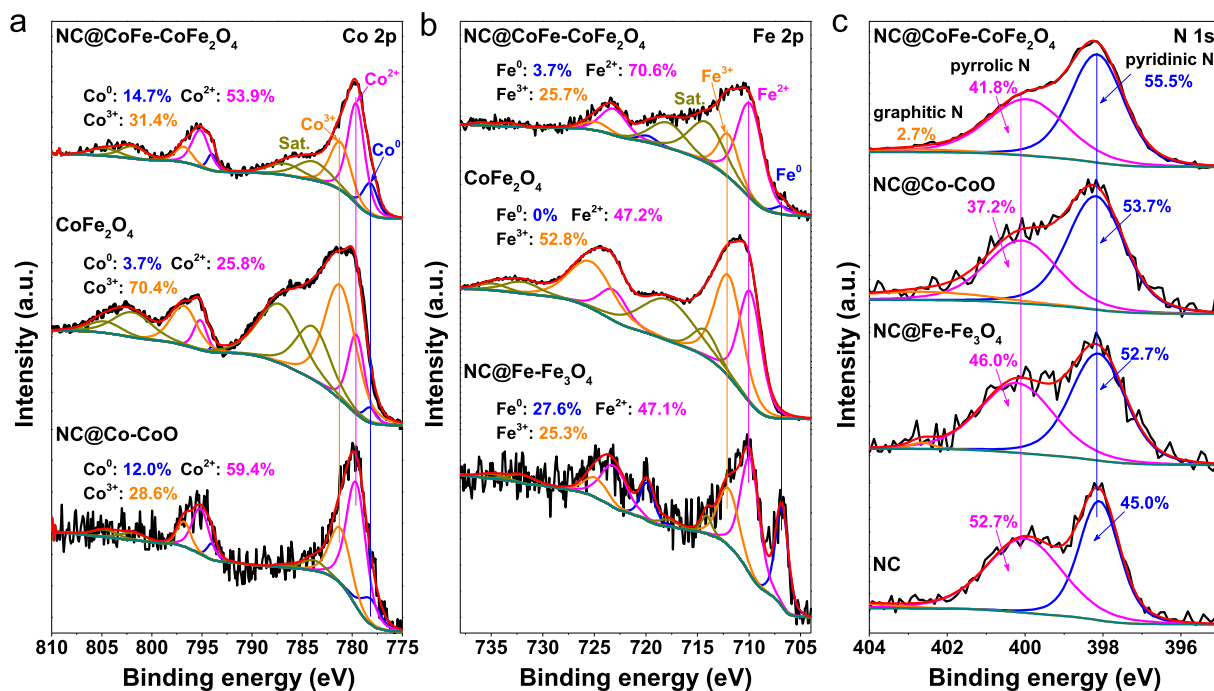

Fig. 3. High-resolution XPS spectra of (a) Co 2p, (b) Fe 2p and (c) N 1s from NC@CoFe−CoFe₂O₄, CoFe₂O₄, NC@Co−CoO, NC@Fe−Fe₃O₄ and NC, respectively.

carbon graphitization. Notably, the NC@CoFe−CoFe$_2$O$_4$ shows a typical signal at 670.4 cm^{-1} belonging to Fe−O [28]. The higher graphitization of NC@CoFe−CoFe$_2$O$_4$ facilitates fast electron transport and thus contributes to improving the catalytic performance.

To evaluate the metal oxide content in NC@CoFe−CoFe$_2$O$_4$, the detailed thermos gravimetric analysis (TGA) was carried out in the O$_2$ atmosphere. As shown in Fig. S4, a small exothermic peak, appeared before 120 °C due to the evaporation of the adsorbed H$_2$O molecules. There is a strong exothermic peak shown at 245.6 °C due to the burning of amorphous carbon, while the exothermic peak at 303.5 °C is the decomposition of graphitized carbon. Therefore, the content of metal oxide is about 34.2 wt%.

3.3. XPS analysis

XPS measurement is a powerful tool to survey the chemical state and electronic structure of the as-prepared materials [29]. As shown in Fig. S5, the full-range XPS survey spectrum of NC@Co-Fe−CoFe$_2$O$_4$ contains the elements of Co, Fe, O, N and C, in which the high-resolution C 1s spectrum is convoluted into four peaks at 284.0 (C=C), 284.8 (C−C/C−N), 286.0 (C−O) and 287.9 eV (C=O), respectively [30,31]. Fig. 3a shows the high-resolution Co 2p core-level spectrum, where the binding energies at 778.2, 779.6, and 781.2 eV of Co 2p$_{3/2}$ can be assigned to the metallic Co, Co^{2+}, and Co^{3+} species, respectively. It can be observed that the contents of metallic Co and Co^{2+} species in the NC coated materials (NC@Co-Fe−CoFe$_2$O$_4$ and NC@Co−CoO) are much higher than these of the

unwrapped material (CoFe$_2$O$_4$). Similar results are also found in the high-resolution Fe 2p spectrum (Fig. 3b), in which the binding energies of Fe 2p$_{3/2}$ located at 706.8, 709.9, and 712.0 eV are ascribed to the metallic Fe, Fe^{2+}, and Fe^{3+} species, respectively. Note: the rest two peaks of Fe 2p$_{3/2}$ at higher binding energies (714.1 and 717.9 eV) are satellite peaks. These results can be interpreted as that the metallic contents of Co and Fe are beneficial to enhance the conductivity of the composite, while Co or Fe could be anchored in the carbon matrix by coordinating with pyridinic N to form Co−N/Fe−N active sites [32,33]. The high-resolution N 1s spectrum of different samples are deconvoluted into three peaks at 398.2, 400.0, and 402.8 eV, which are respectively assigned to pyridinic-N, pyrrolic-N and graphitic-N (Fig. 3c) [34], suggesting that N is indeed doped into the carbon skeletons (Table S2). In addition to the high contents of Co^{2+}/Fe^{2+}, we found that the pyridinic-N in NC-wrapped CoFe−CoFe$_2$O$_4$ catalyst is significantly higher than that of others, further demonstrating the high concentration of Co−N/Fe−N active sites in comparison with other catalysts. This result is consistent with Fe−N$_4$ in Iron porphyria (Fig. S6) [35,36]. Therefore, these high content of Co−N/Fe−N active sites and highly conductive CoFe alloy ensure the improved ORR catalytic performance.

3.4. Electrochemical performance analysis

Pyrolysis temperature is a crucial factor that has been experimentally proven to affect the catalytic activity of ORR [37]. As
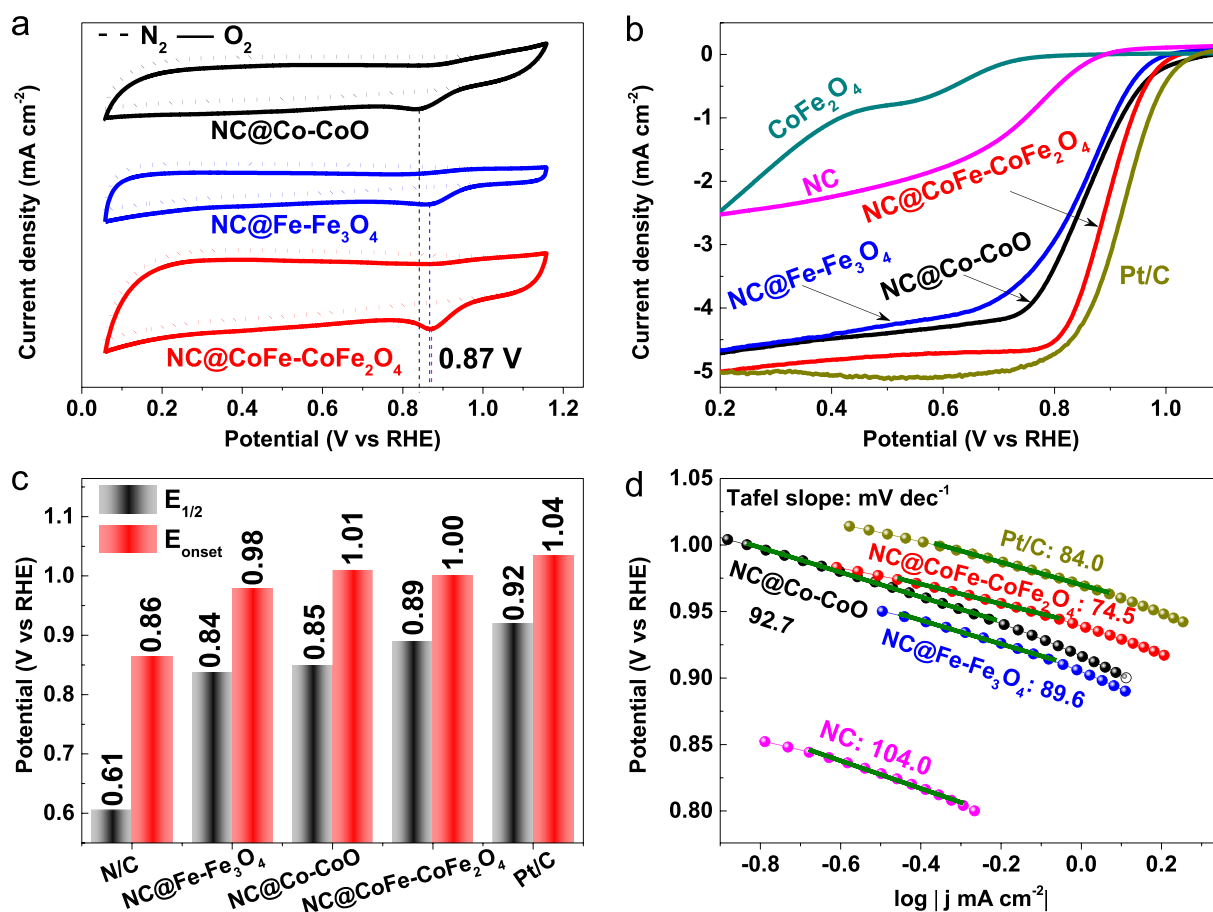

Fig. 4. (a) Cyclic voltammograms (CV) of different catalysts in O$_2$-and N$_2$-saturated KOH electrolyte with a scan rate of 50 mV s^{-1}. (b) Linear sweep voltammograms (LSV) of different catalysts in O$_2$-saturated KOH at 5 mV s^{-1} with a rotation speed of 1600 rpm. (c) The summarized E$_{onset}$ and E$_{1/2}$ from LSV curves. (d) Tafel plots of different catalysts abstracted from LSV curves.

shown in Fig. S7a, the NC@CoFe−CoFe$_2$O$_4$ catalyst synthesized at 700 °C affords a cathodic peak at 0.87 V, which is considerably higher than those of the catalysts synthesized at 600 °C (0.53 V) and 800 °C (0.77 V), indicating that 700 °C is the optimum temperature for synthesizing the ORR catalyst. In addition, the LSV curves of NC@CoFe−CoFe$_2$O$_4$ catalysts synthesized at different temperatures also reveal that the catalyst synthesized at 700 °C has the best ORR activity, with the highest onset potential and maximum limiting current density (Fig. S7b). Therefore, unless otherwise stated, the catalysts discussed below are all prepared at 700 °C.

Fig. 4a shows CVs curves of NC@CoFe−CoFe$_2$O$_4$ catalyst together with NC@Fe−Fe$_3$O$_4$ and NC@Co−CoO as comparison in O$_2$/N$_2$-saturated 0.1 M KOH solution. The NC@CoFe−CoFe$_2$O$_4$ catalyst shows a well-defined cathodic ORR reduction peak at 0.87 V, when it compared in the N$_2$-saturated 0.1 M KOH solution. The result is slightly positive for NC@Fe−Fe$_3$O$_4$ (0.86 V), but still higher than that of NC@Co−CoO (0.84 V) in O$_2$-saturated 0.1 M KOH electrolyte. Fig. 4b is the LSV curves of different catalyst-modified rotating disk electrodes at 1600 rpm in O$_2$-saturated 0.1 M KOH electrolyte. The onset potential (E$_{onset}$) of NC@CoFe−CoFe$_2$O$_4$ catalyst is 1.00 V, which is similar to these of NC-coated Fe/Co-based catalysts and Pt/C catalyst, but much higher than that of CoFe$_2$O$_4$ and NC (Fig. 4c). The half-wave potential (E$_{1/2}$) and limiting current density (−5.0 mA cm^{-2}) of NC@CoFe−CoFe$_2$O$_4$ are close to Pt/C, which are not only far better than these of the control catalysts but also higher than most of the reported literature (Table S3). The smallest Tafel slope of NC@CoFe−CoFe$_2$O$_4$ (74.5 mV dec^{-1}) (Fig. 4d) is the another indication of the faster the protonation of O^{2-} at the active site which is an essential factor determining the reaction rate of ORR [38]. Therefore, one can conclude from this study that the superior

ORR activity is the result of the rich Co−N/Fe−N active sites and good electron conductivity of the metallic CoFe [33].

LSV curves of NC@CoFe−CoFe$_2$O$_4$ in O$_2$-saturated 0.1 M KOH solution at various rotating speeds from 625 to 2500 rpm are recorded through the rotating disk electrode (RDE) measurements (Fig. 5a). Typically, the limiting current density in the LSV curves increases rapidly with increasing electrode rotation rates due to a decreased diffusion distance at high speeds, indicating that the ORR is diffusion-controlled process [39], in accordance with most of the previous studies [40,41]. The K−L plots showed nearly linearity at different potentials, and the electron-transfer numbers (n) are thus calculated to be an average value of 3.94 at potentials ranging from 0.3 V to 0.7 V (Fig. 5b). This results implies that the electrochemical reduction of dissolved O$_2$ follows first-order kinetics, and the O$_2$ reduction by NC@CoFe−CoFe$_2$O$_4$ catalyst is a direct four-electron transfer process [42]. The collected RRDE data in Fig. 5c, and Fig. 5d show that the electron transfer numbers of NC@Co-Fe−CoFe$_2$O$_4$ at different potentials are over 3.8, with yields of H$_2$O$_2$ below 6% throughout the whole potential windows, demonstrating the favorable reduction pathway of oxygen directly to hydroxyl.

According to previous reports, the electrochemical active surface area (EASA) is positively correlated with the electrochemical double-layer capacitance (C$_{dl}$), meaning that higher C$_{dl}$ values have more active sites [27]. Here, the C$_{dl}$ was obtained from CV curves recorded at different scan rates in the non-Faradaic potential region, and the results were shown in Fig. 6a, and Fig. S8. The C$_{dl}$ value of NC@CoFe−CoFe$_2$O$_4$ is 23.57 mF cm^{-2}, which is 1.79− and 9.10−fold higher than those of NC@Co−CoO and NC@Fe−Fe$_3$O$_4$ (Fig. 6b), respectively. The more substantial Cdl value indicates more active sites and thereof resulting in higher ORR catalytic activity.
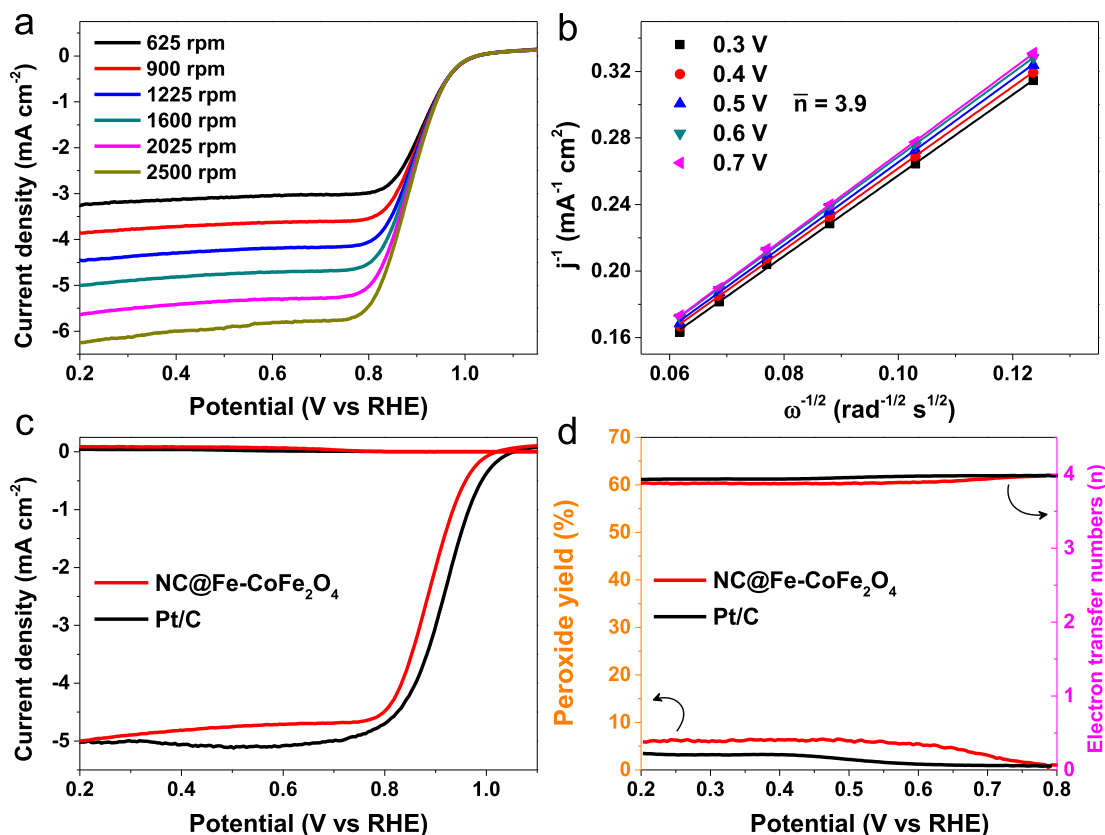

Fig. 5. (a) LSV curves of NC@CoFe−CoFe$_2$O$_4$ catalyst at different rotation rates, and (b) the corresponding Koutecky-Levich plots at different potentials. (c) The LSV curves from RRDE test and (d) the correspondingly summarized peroxide yield and electron transfer numbers (n) of NC@CoFe−CoFe$_2$O$_4$ and Pt/C.
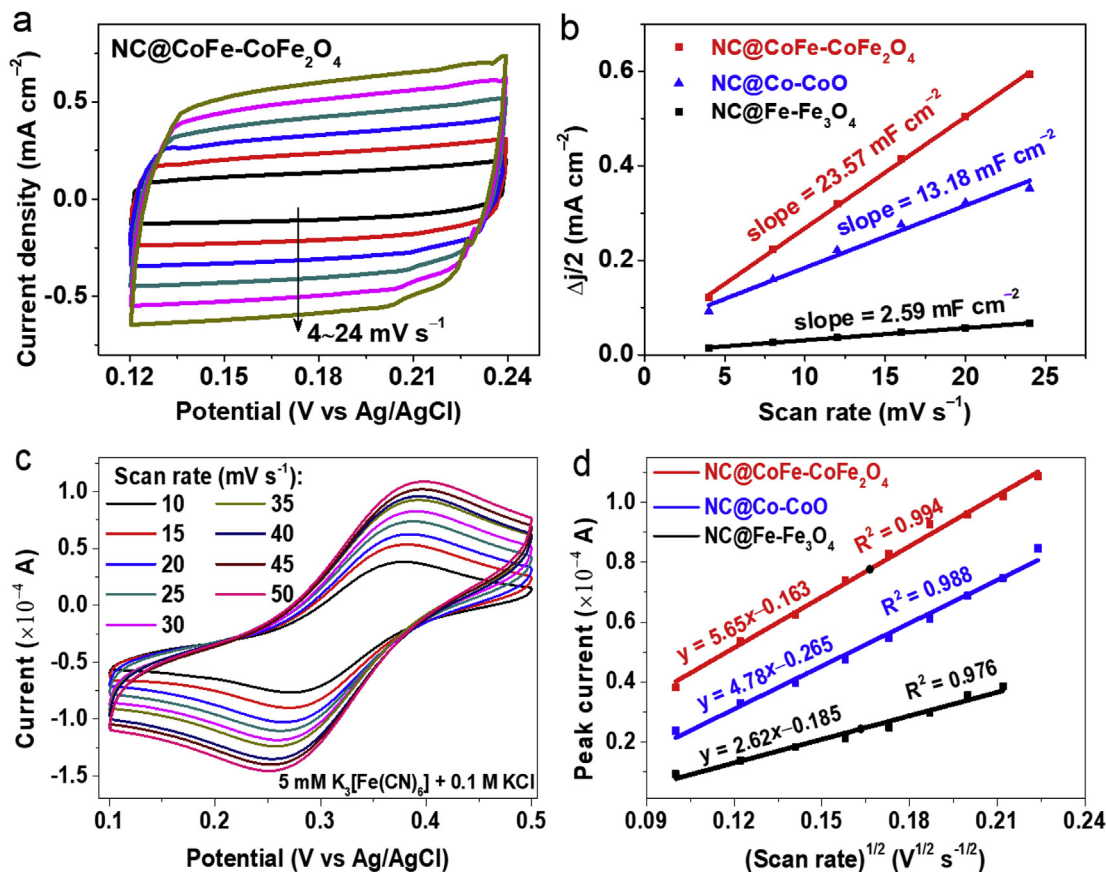
Fig. 6. (a) CV curves of NC@CoFe–CoFe$_2$O$_4$ at different scan rates of 4–24 mV s^{-1} (b) Plots of current density at 0.18 V (vs. Ag/AgCl). versus scan rates of NC@CoFe–CoFe$_2$O$_4$, NC@Co–CoO and NC@Fe–Fe$_3$O$_4$. (c) CV responses of NC@CoFe–CoFe$_2$O$_4$ catalyst in 0.1 M KCl containing 5 mM K$_3$[Fe(CN)$_6$] solution as a function of scan rate from 10 to 50 mV s^{-1}. (d) Linear dependence of peak currents versus square root of san rates for NC@CoFe–CoFe$_2$O$_4$, NC@Co–CoO and NC@Fe–Fe$_3$O$_4$, respectively.

The actual EASA values of different catalysts are further investigated for their association with ORR catalytic activity [43,44]. The specific EASA values of NC@CoFe–CoFe$_2$O$_4$, NC@Fe–Fe$_3$O$_4$, and NC@Co–CoO catalysts are evaluated in 5 mM K$_3$[Fe(CN)$_6$] + 0.1 M KCl solution by using Pt foil as the counter electrode. As shown in Fig. 6c, and Fig. S9, the CV curves show a pair of redox peaks in which the oxidation peaks are plotted against the square root of the scan rates (Fig. 6d). The EASA of NC@CoFe–CoFe$_2$O$_4$ catalyst is *ca.* 4.08 m^2 g^{-1}, which is 2.95– and 5.39–fold higher than these of NC@Co–CoO (1.38 m^2 g^{-1}) and NC@Fe–Fe$_3$O$_4$ (0.76 m^2 g^{-1}), further reflecting the high ORR catalytic activity.

It is established that the SCN$^-$ ion has a high affinity to iron and can poison Co–N/Fe–N coordination sites that are catalyzing ORR [45,46]. As shown in Fig. 7a, the ORR activity of NC@CoFe–CoFe$_2$O$_4$ catalyst is somewhat inhibited with *ca.* 5 mV negative shift for E$_{1/2}$ and severe recession the diffusion-limiting current after the introduction of SCN$^-$ ions, confirming that the Co–N/Fe–N species is the part of active sites in ORR [45,47]. Moreover, the methanol tolerance of NC@CoFe–CoFe$_2$O$_4$ and Pt/C catalysts are further examined by chronoamperometry measurement. It can be seen from Fig. 7b that the catalytic performance of commercial Pt/C is rapidly decreased after the addition of 3.0 M methanol, which is a typical result of poisoning of Pt-based catalysts by CO species [11]. However, in the case of NC@CoFe–CoFe$_2$O$_4$ catalyst, only a slight decline is observed, indicating its excellent resistance towards methanol crossover effect. This gratifying effect can be ascribed to the results of the double protection by CoFe$_2$O$_4$ clusters and NC layers. Therefore, a typical four-electron pathway is proposed to explain the catalytic mechanism [48], where the remarkable ORR

activity has resulted from the synergistic effect of the CoFe alloy enhanced conductivity and the Co–N/Fe–N along with CoFe$_2$O$_4$ based active sites (Fig. S10).

The stability of the NC@CoFe–CoFe$_2$O$_4$ catalyst is evaluated by LSV measurements performed in O$_2$-saturated 0.1 M KOH before and after 2000 cycles. It is observed from Fig. 7c that the E$_{1/2}$ and limiting current density of Pt/C catalyst show a dramatical shift (70 mV) after 2000 cycles. In contrast, the polarization curve of the NC@CoFe–CoFe$_2$O$_4$ catalyst shows a much smaller variation (13 mV) under the same condition (Fig. 7d). The slight decline in activity of NC@CoFe–CoFe$_2$O$_4$ catalyst is primarily related to changes in the chemical states of the surface species. Some of the low-valence Co species are oxidized to Co^{3+}, while part of the high-valence Fe species are reduced to metallic Fe at the same time in alkaline environment (Fig. S11). Once again, these results clearly indicate that the NC@CoFe–CoFe$_2$O$_4$ catalyst has good stability in ORR catalysis and thereof a tremendous commercial application prospects.

4. Conclusions

In summary, a simple and cost-effective strategy is developed for the fabrication of the NC@CoFe–CoFe$_2$O$_4$ catalyst. The resulted NC@CoFe–CoFe$_2$O$_4$ demonstrates an excellent ORR activity and long-term durability, compared to that of the state-of-the-art Pt/C catalyst. Its onset and half-wave potentials are 34 mV and 30 mV negative than those of Pt/C, respectively. Meanwhile, it follows a four-electron pathway dominantly. The experiment results suggest that the combination of sizeable electrochemical area and
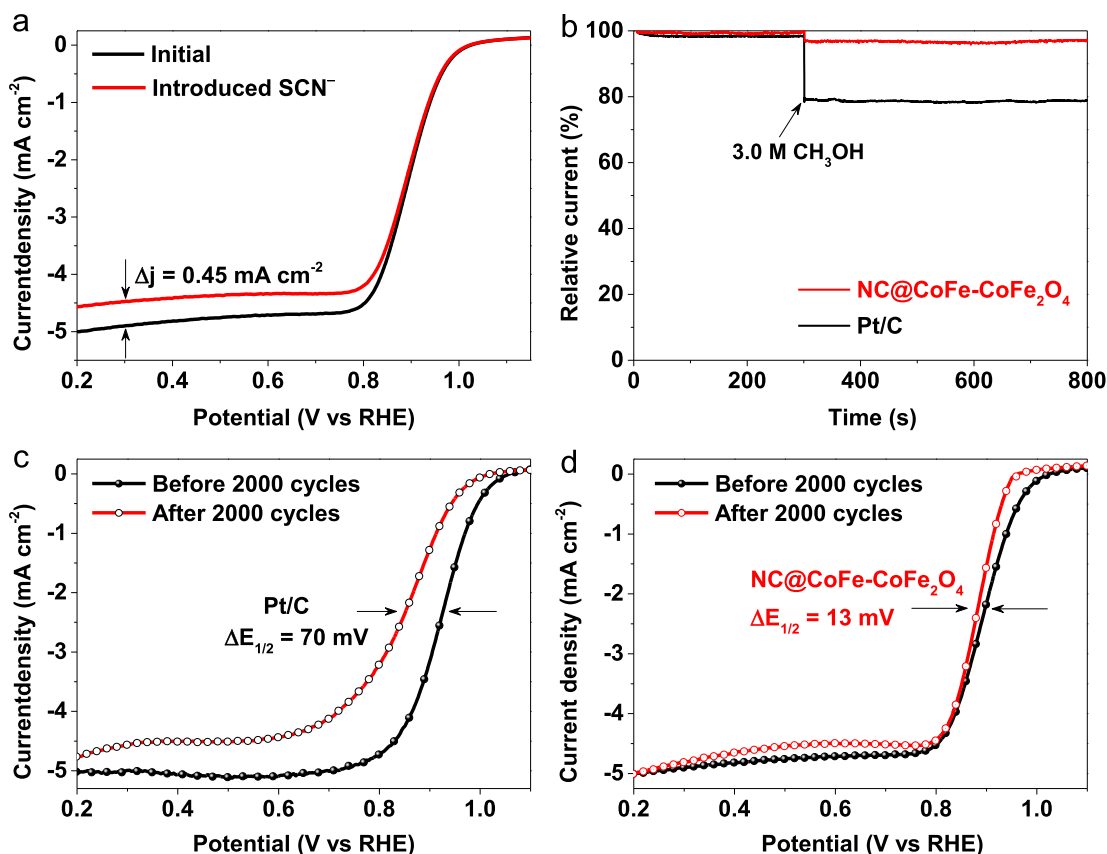
Fig. 7. (a) LSVs of NC@CoFe−CoFe$_2$O$_4$ before and after the addition of 0.1 M KSCN in O$_2$-saturated 0.1 M KOH. (b) The methanol crossover effect test of NC@CoFe−CoFe$_2$O$_4$ and Pt/C upon addition of 3.0 M methanol. LSV curves of (c) commercial Pt/C and (d) NC@CoFe−CoFe$_2$O$_4$ catalysts for ORR before and after 2000 cycles in the potential range of 0.6 V−1.2 V with a scan rate of 50 mV s^{-1} in O$_2$-saturated 0.1 M KOH solution.

multimetal oxides with the N-doped carbon layer may offer more metal-N active sites in comparison with that of single-metal oxides. Contrast experiments have proved that the alloy of CoFe, the doping of N atoms, and the high-crystalline spinel structure of CoFe$_2$O$_4$ are the main contributors to the high ORR activity. The superior methanol-tolerance of the NC@CoFe−CoFe$_2$O$_4$ makes it a promising alternative for costly Pt/C in the methanol fuel cell technology.

Author contribution statement

Mancai Qian: Experimental planning, testing and characterization; **Xiaoyang Cheng:** Experimental planning; **Tingting Sun:** Experimental testing and characterization; **Jianniao Tian:** Experimental supervision; **Tayirjan Taylor Isimjan:** Experimental supervision and writing-reviewing; **Zhongfeng Shi:** Experimental supervision; **Xiulin Yang:** Experimental supervision, writing-reviewing and editing.

Declaration of competing interest

The authors declare that they have no known competing financial interests or personal relationships that could have appeared to influence the work reported in this paper.

Acknowledgements

Appendix A. Supplementary data

Supplementary data to this article can be found online at https://doi.org/10.1016/j.jallcom.2019.153015.

References

[1] X. Liu, L. Wang, P. Yu, C. Tian, F. Sun, J. Ma, W. Li, H. Fu, A stable bifunctional catalyst for rechargeable zinc-air batteries: iron-cobalt nanoparticles embedded in a nitrogen-doped 3D carbon matrix, Angew.Chem. Int. Ed. 57 (2018) 16166−16170.

[2] W. Zhao, K. Huang, Q. Zhang, H. Wu, L. Gu, K. Yao, Y. Shen, Y. Shao, In-situ synthesis, operation and regeneration of nanoporous silver with high performance toward oxygen reduction reaction, Nano Energy 58 (2019) 69−77.

[3] J. Li, S. Mao, Y. Hou, L. Lei, C. Yuan, 3D edge-enriched Fe$_3$C@C nanocrystals with a core-shell structure grown on reduced graphene oxide networks for efficient oxygen reduction reaction, ChemSusChem 11 (2018) 3292−3298.

[4] S. Jiang, K. Ithisuphalap, X.R. Zeng, G. Wu, H.P. Yang, 3D porous cellular NiCoO$_2$/graphene network as a durable bifunctional electrocatalyst for oxygen evolution and reduction reactions, J. Power Sources 399 (2018) 66−75.

[5] L. Huang, Z. Jiang, W. Gong, Z. Wang, P.K. Shen, Two-step etching fabrication of tunable ternary rhombic dodecahedral nanoframes for enhanced oxygen reduction electrocatalysis, J. Power Sources 406 (2018) 42−49.

[6] M. Khandelwal, S. Chandrasekaran, S.H. HurJ, S. Chung, Chemically controlled in-situ growth of cobalt oxide microspheres on N,S-co-doped reduced graphene oxide as an efficient electrocatalyst for oxygen reduction reaction, J. Power Sources 407 (2018) 70−83.

[7] L. Zhang, J. Fischer, Y. Jia, X. Yan, W. Xu, X. Wang, J. Chen, D. Yang, H. Liu, L. Zhuang, M. Hankel, D.J. Searles, K. Huang, S. Feng, C.L. Brown, X. Yao, Coordination of atomic Co-Pt coupling species at carbon defects as active sites

for oxygen reduction reaction, J. Am. Chem. Soc. 140 (2018) 10757—10763.

[8] J. Zhang, Y. Sun, J. Zhu, Z. Kou, P. Hu, L. Liu, S. Li, S. Mu, Y. Huang, Defect and pyridinic nitrogen engineering of carbon-based metal-free nanomaterial toward oxygen reduction, Nano Energy 52 (2018) 307—314.

[9] X. Zhu, R. Amal, X. Lu, N, P Co-coordinated manganese atoms in mesoporous carbon for electrochemical oxygen reduction, Small 15 (2019), e1804524.

[10] S.L. Zhang, B.Y. Guan, X.W.D. Lou, Co-Fe alloy/N-doped carbon hollow spheres derived from dual metal-organic frameworks for enhanced electrocatalytic oxygen reduction, Small 15 (2019), e1805324.

[11] Z. Huang, H. Pan, W. Yang, H. Zhou, N. Gao, C. Fu, S. Li, H. Li, Y. Kuang, In situ self-template synthesis of Fe-N-doped double-shelled hollow carbon microspheres for oxygen reduction reaction, ACS Nano 12 (2018) 208—216.

[12] S.J. Kim, J. Mahmood, C. Kim, G.F. Han, S.W. Kim, S.M. Jung, G. Zhu, J.J. De Yoreo, G. Kim, J.B. Baek, Defect-Free encapsulation of Fe^0 in 2D fused organic networks as a durable oxygen reduction electrocatalyst, J. Am. Chem. Soc. 140 (2018) 1737—1742.

[13] H. Hu, B. Guan, B. Xia, X.W. Lou, Designed formation of $Co_3O_4/NiCo_2O_4$ double-shelled nanocages with enhanced pseudocapacitive and electrocatalytic properties, J. Am. Chem. Soc. 137 (2015) 5590—5595.

[14] X.J. Lei Lu, Jiawei Fan, Wu Lei, Yu Ouyang, Xifeng Xia, Zhixin Xue, Q. Hao, Cobalt ferrite on honeycomb-like algae-derived nitrogen-doped carbon for electrocatalytic oxygen reduction and ultra-cycle-stable lithium storage, Electrochim. Acta 295 (2019) 461—471.

[15] K. Mohanraju, V. Sreejith, R. Ananth, L. Cindrella, Enhanced electrocatalytic activity of PANI and $CoFe_2O_4$/PANI composite supported on graphene for fuel cell applications, J. Power Sources 284 (2015) 383—391.

[16] C. Ren, K. Li, C. Lv, Y. Zhao, J. Wang, S. Guo, Nanorod $CoFe_2O_4$ modified activated carbon as an efficient electrocatalyst to improve the performance of air cathode microbial fuel cell, J. Electroanal. Chem. 840 (2019) 134—143.

[17] Q. Kang-Wen, C. Xi, Y. Zhang, R. Zhang, Z. Li, G.-R. Sheng, H. Liu, C.-K. Dong, Y.-J. Chen, X.-W. Du, Laser-induced oxygen vacancies in $FeCo_2O_4$ nanoparticles for boosting oxygen evolution and reduction, Chem. Commun. 55 (2019) 8579—8582.

[18] N. Xu, Y. Zhang, T. Zhang, Y. Liu, J. Qiao, Efficient quantum dots anchored nanocomposite for highly active ORR/OER electrocatalyst of advanced metal-air batteries, Nano Energy 57 (2018) 176—185.

[19] Q. Qin, L. Chen, T. Wei, Y. Wang, X. Liu, Ni/NiM_2O_4 (M = Mn or Fe) supported on N-doped carbon nanotubes as trifunctional electrocatalysts for ORR, OER and HER, Catal. Sci. Technol 9 (2019) 1595—1601.

[20] X. Jia, Y. Zhang, L. Zhang, L. Wang, L. Zhou, Fabrication and bifunctional electrocatalytic performance of $FeNi_3/MnFe_2O_4$/nitrogen-doping reduced graphene oxide nanocomposite for oxygen electrocatalytic reactions, Ionics (2019), https://doi.org/10.1007/s11581-019-03251-7.

[21] Y. Niu, X. Huang, L. Zhao, W. Hu, C.M. Li, One-Pot synthesis of $Co/CoFe_2O_4$ nanoparticles supported on N-doped graphene for efficient bifunctional oxygen electrocatalysis, ACS Sustain. Chem. Eng. 6 (2018) 3556—3564.

[22] Z. Tan, H. Li, Q. Feng, L. Jiang, H. Pan, Z. Huang, Q. Zhou, H. Zhou, S. Ma, Y. Kuang, One-pot synthesis of Fe/N/S-doped porous carbon nanotubes for efficient oxygen reduction reaction, J. Mater. Chem. A 7 (2019) 1607—1615.

[23] Y. Han, P. Li, J. Liu, S. Wu, Y. Ye, Z. Tian, C. Liang, Strong Fe^{3+}-O(H)-Pt interfacial interaction induced excellent stability of Pt/NiFe-LDH/rGO electrocatalysts, Sci. Rep. 8 (2018) 1359.

[24] Z. Lu, W. Xu, W. Zhu, Q. Yang, X. Lei, J. Liu, Y. Li, X. Sun, X. Duan, Three-dimensional NiFe layered double hydroxide film for high-efficiency oxygen evolution reaction, Chem. Commun. 50 (2014) 6479—6482.

[25] H. Jin, H. Zhou, W. Li, Z. Wang, J. Yang, Y. Xiong, D. He, L. Chen, S. Mu, In situ derived Fe/N/S-codoped carbon nanotubes from ZIF-8 crystals as efficient electrocatalysts for the oxygen reduction reaction and zinc—air batteries, J. Mater. Chem. A 6 (2018) 20093—20099.

[26] G. Ren, L. Gao, C. Teng, Y. Li, H. Yang, J. Shui, X. Lu, Y. Zhu, L. Dai, Ancient chemistry "pharaoh's snakes" for efficient Fe-/N-doped carbon electrocatalysts, ACS Appl. Mater. Interfaces 10 (2018) 10778—10785.

[27] J.Q. Sun, D.J. Yang, S. Lowe, L.J. Zhang, Y.Z. Wang, S.L. Zhao, P.R. Liu, Y. Wang, Z.Y. Tang, H.J. Zhao, X.D. Yao, Sandwich-Like reduced graphene oxide/carbon black/amorphous cobalt borate nanocomposites as bifunctional cathode electrocatalyst in rechargeable zinc-air batteries, Adv. Energy Mater. 8 (2018) 1801495.

[28] Y. Zhang, G. Zhang, W. Li, X. Li, K. Uchiyama, C. Chen, Enhancing oxygen reduction activity by exposing (111) facets of $CoFe_2O_4$ octahedron on graphene, ChemistrySelect 2 (2017) 9878—9881.

[29] S. Liu, H. Zhang, X. Mu, C. Chen, Surface reconstruction engineering of twinned Pd_2CoAg nanocrystals by atomic vacancy inducement for hydrogen evolution

[30] Q. Gan, X. Cheng, J. Chen, D. Wang, B. Wang, J. Tian, T.T. Isimjan, X. Yang, and oxygen reduction reactions, Appl. Catal., B 241 (2019) 424—429.

[30] Q. Gan, X. Cheng, J. Chen, D. Wang, B. Wang, J. Tian, T.T. Isimjan, X. Yang, Temperature effect on crystallinity and chemical states of nickel hydroxide as alternative superior catalyst for urea electrooxidation, Electrochim. Acta 301 (2019) 47—54.

[31] C. Wu, J. Guo, J. Zhang, Y. Zhao, J. Tian, T.T. Isimjan, X. Yang, Palladium nanoclusters decorated partially decomposed porous ZIF-67 polyhedron with ultrahigh catalytic activity and stability on hydrogen generation, Renew. Energy 136 (2019) 1064—1070.

[32] H. Li, Z. Zhang, M. Dou, F. Wang, Towards high-performance electrocatalysts for oxygen reduction: inducing atomic-level reconstruction of $Fe-n_x$ site for atomically dispersed Fe/N-doped hierarchically porous carbon, Chem. Eur. J. 24 (2018) 8848—8856.

[33] T. Feng, M. Zhang, A mixed-ion strategy to construct CNT-decorated Co/N-doped hollow carbon for enhanced oxygen reduction, Chem. Commun. 54 (2018) 11570—11573.

[34] T. Feng, H. Qin, M. Zhang, Co@C nanoparticle embedded hierarchically porous N-doped hollow carbon for efficient oxygen reduction, Chem. Eur J 24 (2018) 10178—10185.

[35] J.-C. Li, Z.-Q. Yang, D.-M. Tang, L. Zhang, P.-X. Hou, S.-Y. Zhao, C. Liu, M. Cheng, G.-X. Li, F. Zhang, H.-M. Cheng, N-doped carbon nanotubes containing a high concentration of single iron atoms for efficient oxygen reduction, NPG Asia Mater. 10 (2018) e461.

[36] C. Zhang, J. Liu, Y. Ye, Z. Aslam, R. Brydson, C. Liang, Fe-N-Doped mesoporous carbon with dual active sites loaded on reduced graphene oxides for efficient oxygen reduction catalysts, ACS Appl. Mater. Interfaces 10 (2018) 2423—2429.

[37] H. Peng, Z. Mo, S. Liao, H. Liang, L. Yang, F. Luo, H. Song, Y. Zhong, B. Zhang, High performance Fe- and N- doped carbon catalyst with graphene structure for oxygen reduction, Sci. Rep. 3 (2013) 1765.

[38] D. Guo, S. Han, J. Wang, Y. Zhu, MIL-100-Fe derived N-doped Fe/Fe3C@C electrocatalysts for efficient oxygen reduction reaction, Appl. Surf. Sci. 434 (2018) 1266—1273.

[39] B.B. Huang, Y.C. Liu, X. Huang, Z.L. Xie, Multiple heteroatom-doped few-layer carbons for the electrochemical oxygen reduction reaction, J. Mater. Chem. A 6 (2018) 22277—22286.

[40] Y. Zhao, J. Wan, H. Yao, L. Zhang, K. Lin, L. Wang, N. Yang, D. Liu, L. Song, J. Zhu, L. Gu, L. Liu, H. Zhao, Y. Li, D. Wang, Few-layer graphdiyne doped with sp-hybridized nitrogen atoms at acetylenic sites for oxygen reduction electrocatalysis, Nat. Chem. 10 (2018) 924—931.

[41] J. Han, G. Huang, Z. Wang, Z. Lu, J. Du, H. Kashani, M. Chen, Low-temperature carbide-mediated growth of bicontinuous nitrogen-doped mesoporous graphene as an efficient oxygen reduction electrocatalyst, Adv. Mater. 30 (2018) 1803588.

[42] Y. Zeng, S. Tian, D. Wang, H. Dong, X. Cheng, Y. Zhao, J. Tian, X. Yang, Facile synthesis of polyhedral Pd nanocrystals as a highly active and methanol-tolerant electrocatalyst for oxygen reduction, ChemistrySelect 2 (2017) 9291—9297.

[43] H.-W. Liang, W. Wei, Z.-S. Wu, X. Feng, K. Müllen, Mesoporous metal—nitrogen-doped carbon electrocatalysts for highly efficient oxygen reduction reaction, J. Am. Chem. Soc. 135 (2013) 16002—16005.

[44] H. Tan, J. Tang, J. Henzie, Y. Li, X. Xu, T. Chen, Z. Wang, J. Wang, Y. Ide, Y. Bando, Y. Yamauchi, Assembly of hollow carbon nanospheres on graphene nanosheets and creation of iron—nitrogen-doped porous carbon for oxygen reduction, ACS Nano 12 (2018) 5674—5683.

[45] Y. Chen, S. Ji, Y. Wang, J. Dong, W. Chen, Z. Li, R. Shen, L. Zheng, Z. Zhuang, D. Wang, Y. Li, Isolated single iron atoms anchored on N-doped porous carbon as an efficient electrocatalyst for the oxygen reduction reaction, Angew. Chem. Int. Ed. 56 (2017) 6937—6941.

[46] W.J. Jiang, L. Gu, L. Li, Y. Zhang, X. Zhang, L.J. Zhang, J.Q. Wang, J.S. Hu, Z. Wei, L.J. Wan, Understanding the high activity of Fe-N-C electrocatalysts in oxygen reduction: Fe/Fe3C nanoparticles boost the activity of $Fe-n_x$, J. Am. Chem. Soc. 138 (2016) 3570—3578.

[47] J.-D. Yi, R. Xu, Q. Wu, T. Zhang, K.-T. Zang, J. Luo, Y.-L. Liang, Y.-B. Huang, R. Cao, Atomically dispersed iron—nitrogen active sites within porphyrinic triazine-based frameworks for oxygen reduction reaction in both alkaline and acidic media, ACS Energy Lett. 3 (2018) 883—889.

[48] X. Cheng, P. Yan, S. Liu, M. Qian, B. Wang, Z. Wan, J. Tian, X.-C. Shen, T.T. Isimjan, X. Yang, Well-dispersed iron oxide stabilized $Fe-N_4$ active sites in porous N-doped carbon spheres as alternative superior catalyst for oxygen reduction, Int. J. Hydrogen Energy 44 (2019) 12127—12137.